

Error Signals for Overcoming the Laser Power Limits of Gravitational-Wave Detection

Liu Tao,¹ Pooyan Goodarzi,¹ and Jonathan W. Richardson^{1,*}

¹*Department of Physics & Astronomy, University of California, Riverside, Riverside, CA 92521 USA*

(Dated: September 9, 2025)

A major barrier to improving the quantum-limited sensitivity of gravitational-wave observatories are the thermal distortions of the test masses which arise at megawatt laser power. Recent advances in a new form of higher-order wavefront correction, in which corrective heating profiles are applied to the test mass surfaces near their edges, have the potential to enable a tenfold reduction of the quantum noise floor of future detectors. However, realizing high levels of quantum noise reduction in practice hinges on identifying measurable error signals to finely control each wavefront actuator, in order to suppress wavefront errors to few-nanometer precision across the full mirror apertures. No direct source of such an error signal exists in LIGO today. We demonstrate that thermally imaging the surface of each test mass can provide these critical error signals. We show that the surface temperature profiles obtained from thermal imaging can be uniquely mapped to a finite element model of the mirror whose complete thermal state is identified, enabling full-aperture wavefront reconstruction and direct error signals for real-time precision wavefront control. This new sensing capability can enable up to a 34% strain sensitivity improvement in LIGO A+ at 95% confidence, increasing the sky-averaged detection range for binary neutron star mergers by 11 Mpc, and will be integral to a next-generation 40-km gravitational-wave observatory in the U.S., Cosmic Explorer.

I. INTRODUCTION

Since the first detection of gravitational waves from two coalescing black holes in 2015 [1], the Laser Interferometer Gravitational-Wave Observatory (LIGO) and the European Virgo observatory have opened a new means of observing the Universe, launching an era of multi-messenger astronomy. A wide variety of merger events involving black holes and neutron stars have now been observed [2–5]. The path to opening a much broader range of observational science, from precision cosmology [6, 7] to direct tests of strong-field general relativity [8–10] and dense nuclear matter [11], now lies in reducing the instrumental noise floor of gravitational-wave detectors.

LIGO plans to incorporate technical improvements in two major upgrades of the 4-km detectors, LIGO A+ [12] followed by LIGO A# [13, 14]. The A+ upgrades are aimed primarily at reducing thermal noise through improved optical coatings. The A# upgrades will include larger 100-kg test masses, new improved suspensions, and significantly higher levels of circulating laser power and quantum squeezing [15, 16]. Together, these upgrades will demonstrate the key technology for a next-generation 40-km gravitational-wave observatory in the U.S., Cosmic Explorer [17]. With 320-kg test masses and a tenfold longer arm length, Cosmic Explorer will push the gravitational-wave detection horizon to near the edge of the observable Universe, detecting hundreds of thousands to millions of compact binary merger events per year.

Quantum noise, arising from the quantum nature of the laser field [18, 19], is the limiting source of instrumental noise across most of the frequency band accessible to ground-based gravitational-wave detectors. Amplitude-quadrature fluctuations of the laser field displace the

test masses through radiation pressure, introducing significant noise at low frequencies (below 20 Hz). Phase-quadrature fluctuations of the laser field also manifest as shot noise in the detector’s phase-sensitive readout signal. Photon shot noise limits LIGO’s strain sensitivity at all frequencies above 200 Hz. In order to reach their strain sensitivity targets, the LIGO A# and Cosmic Explorer detectors must achieve significantly greater levels of quantum noise reduction, requiring an unprecedented 1.5 MW of circulating laser power in their arm cavities and 10 dB of frequency-dependent squeezing [13, 17].

The achievable arm power and squeezing are limited, in practice, by thermal distortions of the test masses [20]. In recent work [21], we reported the potential of a new class wavefront actuator, known as the FROnt Surface Type Irradiator (FROSTI), to enable next-generation quantum noise targets when used to augment LIGO’s existing thermal compensation capabilities [22]. However, *realizing* the potential sensitivity improvements of Ref. [21] relies on there also existing error signals to precisely identify the optimal power settings of the wavefront actuators, so as to minimize root mean square (RMS) wavefront errors across the full aperture of the mirrors. No direct error signals containing full-aperture wavefront information exist in LIGO today. LIGO’s existing Hartmann wavefront sensors [22], for example, are fundamentally limited in their field of view to only the central region of the test masses. Similarly, Virgo employs phase cameras as wavefront sensors to measure the spatial structure of the laser fields, but these systems also suffer from a limited field of view due to the limited beam size [23].

In this letter, we present a novel sensing technique that can provide these critical error signals using thermal imaging cameras. We describe this sensing technique in §II and demonstrate its feasibility in §III, assuming realistic sensor resolution limits. We then show in §IV that the improved capability provided by this technique to infer,

* jonathan.richardson@ucr.edu

and thus to more finely correct, thermally-driven wavefront errors in gravitational-wave detectors will significantly improve their quantum-limited strain sensitivity, which we find can be improved up to 34% in LIGO A+. Finally, we discuss the enabling impact of this work on future gravitational-wave detectors, beyond A+, in §V.

II. THERMAL STATE INFERENCE

We aim to *uniquely* and *accurately* infer the full thermal state of each test mass directly from the temperature profile of its front (reflective-coated) surface. This surface temperature map is measured *in situ* using a thermal imaging camera, located outside the vacuum system, and matched to a finite element analysis (FEA) thermal model of the test mass. As illustrated in Fig. 1, the thermal steady state is fully characterized by five parameters: the power absorbed from the 1064-nm laser beam, P_S ; the beam's location on the test mass, (x_0, y_0) , which in general can be offset from the center; and the absorbed powers delivered by two different wavefront actuators. The actuators include LIGO's existing ring heater [24], which projects a heating power of P_R onto the barrel of the test mass to correct defocus (radius of curvature) error, and the recently proposed FROnt Surface Type Irradiator (FROSTI) [21], which projects an annular heating pattern of power P_F onto the front surface of the test mass, near the edge, to correct higher-order aberrations. These parameters are summarized in Table I.

In the steady state, the two-dimensional surface temperature map measured by the thermal imaging camera, $T(x, y)$, can be decomposed into a linear combination of contributions from each of the three thermal sources:

$$T(x, y) = P_S \hat{T}_S(x, y | x_0, y_0) + P_R \hat{T}_R(x, y) + P_F \hat{T}_F(x, y) \quad (1)$$

The functions $\hat{T}_R(x, y)$ and $\hat{T}_F(x, y)$ respectively represent the surface temperature maps due to the ring heater and FROSTI actuators delivering unit power. Similarly, the function $\hat{T}_S(x, y | x_0, y_0)$ represents the surface temperature map due to unit power absorbed from the incident laser beam, whose centroid is located at position (x_0, y_0) relative to the center of the test mass. We refer to \hat{T}_S , \hat{T}_R , and \hat{T}_F as unit temperature maps or “unit maps.” The linear addition of these units maps assumed in Eq. 1 is confirmed by FEA modeling to be valid at the power levels of interest ($P_S \sim 1$ W and $P_R \sim P_F \sim 10$ W).

We can infer the values of the three absorbed powers by computing the spatial overlap integrals of the measured temperature map with each unit map. For succinctness, we adopt a bra-ket notation to represent the spatial overlap integral of any two temperature maps, T_α and T_β , as

$$\langle T_\alpha | T_\beta \rangle = \iint T_\alpha(x, y) T_\beta(x, y) dx dy \quad (2)$$

evaluated over the entire surface of the test mass. The spatial overlap integral of the measured temperature map

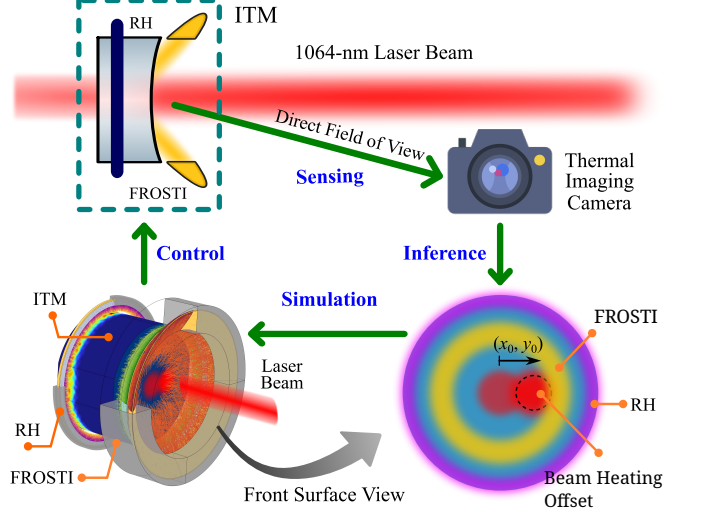


FIG. 1. Test mass thermal state inference from front-surface thermal imaging. It is used to infer the parameters in Table I.

Parameter	Units	Description
P_S	W	Power absorbed from laser beam
x_0	mm	Laser beam centroid x -coordinate
y_0	mm	Laser beam centroid y -coordinate
P_R	W	Power delivered by ring heater
P_F	W	Power delivered by FROSTI

TABLE I. Parameters defining the thermal steady state of one test mass. Each parameter is described further in §II.

(Eq. 1) with any unit map, \hat{T}_α , can thus be expressed as

$$\langle \hat{T}_\alpha | T \rangle = P_S \langle \hat{T}_\alpha | \hat{T}_S \rangle + P_R \langle \hat{T}_\alpha | \hat{T}_R \rangle + P_F \langle \hat{T}_\alpha | \hat{T}_F \rangle \quad (3)$$

where the explicit dependence of \hat{T}_S on the laser beam's position, (x_0, y_0) , is dropped but remains implied.

Evaluating Eq. 3 for all three unit maps yields the matrix equation

$$\begin{pmatrix} \langle \hat{T}_S | T \rangle \\ \langle \hat{T}_R | T \rangle \\ \langle \hat{T}_F | T \rangle \end{pmatrix} = \begin{pmatrix} \langle \hat{T}_S | \hat{T}_S \rangle & \langle \hat{T}_S | \hat{T}_R \rangle & \langle \hat{T}_S | \hat{T}_F \rangle \\ \langle \hat{T}_R | \hat{T}_S \rangle & \langle \hat{T}_R | \hat{T}_R \rangle & \langle \hat{T}_R | \hat{T}_F \rangle \\ \langle \hat{T}_F | \hat{T}_S \rangle & \langle \hat{T}_F | \hat{T}_R \rangle & \langle \hat{T}_F | \hat{T}_F \rangle \end{pmatrix} \begin{pmatrix} P_S \\ P_R \\ P_F \end{pmatrix} \quad (4)$$

which can be inverted to obtain an expression for the absorbed powers from the three thermal sources:

$$\begin{pmatrix} P_S \\ P_R \\ P_F \end{pmatrix} = \begin{pmatrix} \langle \hat{T}_S | \hat{T}_S \rangle & \langle \hat{T}_S | \hat{T}_R \rangle & \langle \hat{T}_S | \hat{T}_F \rangle \\ \langle \hat{T}_R | \hat{T}_S \rangle & \langle \hat{T}_R | \hat{T}_R \rangle & \langle \hat{T}_R | \hat{T}_F \rangle \\ \langle \hat{T}_F | \hat{T}_S \rangle & \langle \hat{T}_F | \hat{T}_R \rangle & \langle \hat{T}_F | \hat{T}_F \rangle \end{pmatrix}^{-1} \begin{pmatrix} \langle \hat{T}_S | T \rangle \\ \langle \hat{T}_R | T \rangle \\ \langle \hat{T}_F | T \rangle \end{pmatrix} \quad (5)$$

An FEA thermal model of the test mass is used to calculate each unit map, from which the 3×3 matrix of overlap coefficients in Eq. 5 can be numerically calculated.

Although the beam heating unit map in Eq. 5, \hat{T}_S , depends on the beam's unknown position on the test mass,

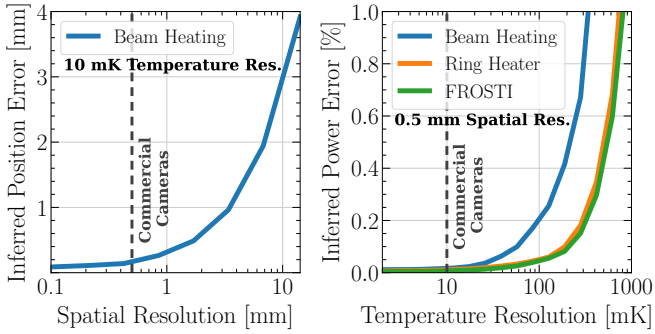


FIG. 2. Performance of the thermal state inference algorithm. *Left:* Error of the inferred radial position of the laser beam, as a function of the spatial resolution of the thermal image. *Right:* Relative errors of the inferred powers, as a function of the temperature resolution of the thermal image.

the absorbed powers and the beam position can be jointly inferred via an iterative procedure. First, we solve Eq. 5 assuming that the beam is perfectly centered, using the unit map $\hat{T}_S(x, y | 0, 0)$. Second, using these initial estimates of the absorbed powers, we subtract the ring heater and FROSTI contributions from the measured temperature map to obtain a residual map representing the beam heating. We estimate the *true* position of the beam's centroid as the location of the global maximum in this residual temperature map. Third, we solve Eq. 5 again using the beam heating unit map for the estimated centroid, $\hat{T}_S(x, y | x_0, y_0)$. Thus, we obtain an estimate of the actual beam position on the test mass, (x_0, y_0) , from step 2 and then use this to refine our estimate of the absorbed powers, P_S , P_R , and P_F , in step 3. With knowledge of these five parameters, we can use an FEA thermal model of the test mass with their specific values to generate full-aperture mirror phase maps of the *actual* wavefront errors in reflection and transmission. These phase maps provide a direct error signal for optimizing the ring heater and FROSTI power settings for each test mass.

III. MODEL PERFORMANCE

To assess the inferential power of our model, we trial it on a set of simulated thermal images generated by an FEA model of a test mass with all three thermal sources. We assume absorbed powers similar to those expected at 1.5 MW of arm power in LIGO A#: $P_S = 1$ W of power is absorbed by the front surface of the test mass from the incident laser beam, $P_R = 20$ W of power is absorbed by the barrel of the test mass from a ring heater heating profile matching the current LIGO design [24], and $P_F = 10$ W of power is absorbed by the front surface of the test mass from a FROSTI heating profile matching the O5 prototype design [25]. The simulated thermal images are generated at these fixed levels of absorbed power, with the incident laser beam radially offset from the test mass center by an increasing amount up to 2 cm.

Fig. 2 shows the model's ability to accurately recover the true thermal state of the test mass, as the spatial and temperature resolutions of the thermal imaging camera are varied. The left panel shows the average error on the inferred radial position of the laser beam as a function of the spatial resolution (pixelation scale) of the image. The right panel shows the average relative errors on the inferred power levels of the contributing thermal sources as a function of the temperature resolution of the image. We find that a commercial thermal imaging camera, with a 600×600 pixel array and a temperature resolution of 10 mK (indicated by the dashed vertical lines in Fig. 2), paired with an appropriate set of image relay lenses can accurately recover the true beam position to better than 0.5 mm and the true power levels to better than 0.1% for all thermal sources. The feasibility of similar thermal imaging systems has already been demonstrated in Virgo to monitor for point absorbers on the test masses [26].

IV. ASTROPHYSICAL IMPACT

Enhancing our ability to infer, and thus to more finely correct, thermally-driven wavefront errors in LIGO will directly improve its astrophysical sensitivity. To quantify this, we perform head-to-head Monte Carlo optical simulations of a LIGO A+ detector [27] with and without the proposed new sensing capabilities using FINESSE [28], following the procedure in Ref. [21]. We integrate FEA thermal models of each test mass into the simulation to apply mirror phase maps due to laser beam heating, ring heater thermal actuation, and FROSTI thermal actuation. The laser beam heating is modeled assuming a uniform coating absorption of 0.5 ppm for each test mass. LIGO's existing compensation plates [24] are included in the FEA model of the input test masses (ITMs), but we fix the 10.6- μm laser heating power to zero based on the optimal setting from the prior study [21] and the design goal of phasing them out entirely in Cosmic Explorer.

Given a true set of wavefront errors due to laser beam heating, we use Monte Carlo to simulate our practical inability to perfectly *resolve* those wavefront errors, which thus limits the precision to which we can identify the optimal power settings of the wavefront actuators and the optimal beam positions. In each trial, we randomly sample the laser beam position, the ring heater power setting, and the FROSTI power setting on each of the four test masses. These parameters are drawn from independent Gaussian distributions centered on their optimal values, corresponding to perfectly centered beams and the wavefront actuator powers which minimize the full-aperture RMS wavefront errors. The standard deviation of each parameter is chosen to match the level of inferential uncertainty in practically *determining* its optimal value.

For the case with thermal imaging of the test masses, we adopt 3σ distribution widths of 0.5 mm for the beam positional uncertainties and 0.1% for the ring heater and FROSTI power uncertainties, based on the findings in

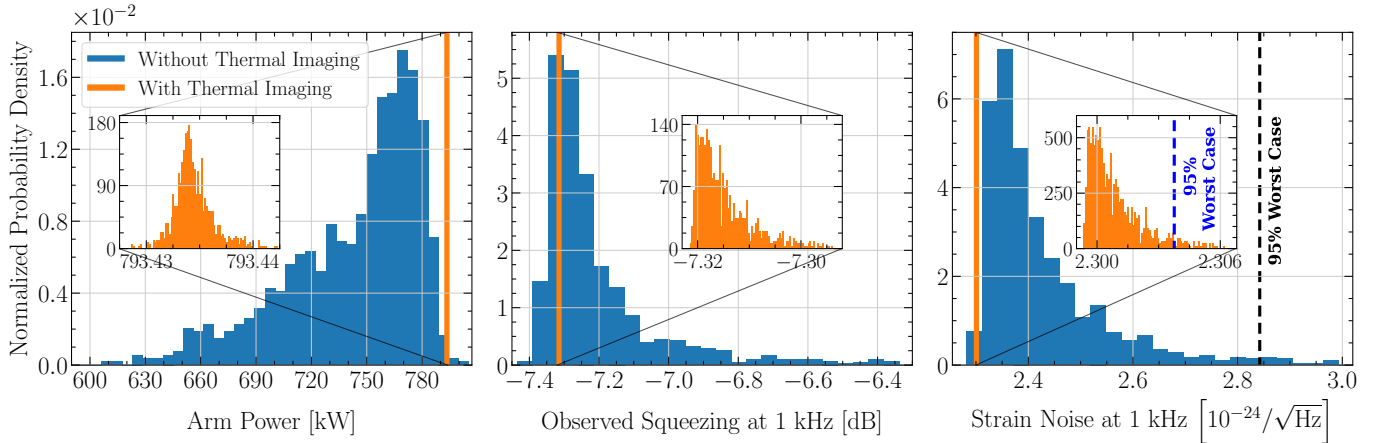


FIG. 3. Distributions of the performance of a LIGO A+ detector with realistic uncertainties in the beam positions and the optimal power settings of the wavefront actuators. *Left:* The achievable power in the arm cavities, with a fixed input power of 125 W. *Middle:* The observed quantum squeezing level at 1 kHz, with a fixed effective input level of 9 dB. *Right:* The resulting total quantum-limited strain noise at 1 kHz. The dashed vertical lines indicate the worst possible outcomes at 95% confidence.

§III. For the case without thermal imaging, we assume the same inference is performed using only signals available in LIGO today. Accordingly, we adopt a 3σ distribution width of 1 mm for the beam positional uncertainties, based on the current best knowledge provided by infrared cameras [29]. The laser power absorbed by each test mass can be estimated as the product of the arm power, with an average calibration uncertainty of 3.1% [30], and the absorptivity of the reflective coating, with an average measurement uncertainty of 31.4% [31]. This yields a total relative uncertainty of 35.5% in the power absorbed by each test mass, which we adopt as the 3σ distribution width of the ring heater and FROSTI powers.

Fig. 3 shows the projected impact of the new wavefront sensing capabilities on the key performance metrics that determine LIGO’s quantum-limited sensitivity. The two cases, with (orange) and without (blue) thermal imaging of the test masses, are each obtained from roughly 1000 Monte Carlo trials assuming the inferential uncertainties described above. We find that 1000 trials are adequate to fully sample the distributions, based on convergence testing of their 95th percentiles. The left panel shows the probability distributions of laser power in the detector’s arm cavities for a fixed input power of 125 W. The middle panel show the probability distributions of observed squeezing at 1 kHz for a fixed injected squeezing level of 9 dB, an effective level chosen to account for all attenuation losses and phase noise from the A+ squeezer system. The right panel shows the probability distributions of total resulting strain noise at 1 kHz. There exist cases in which trade-offs between optimizing the arm power (via the power recycling cavity coupling) and squeezing (via the signal recycling cavity coupling) lead to slightly better performance in one of these metrics, individually, without thermal imaging. However, the overall quantum noise performance is consistently improved when thermal imaging is employed, as shown in the rightmost panel.

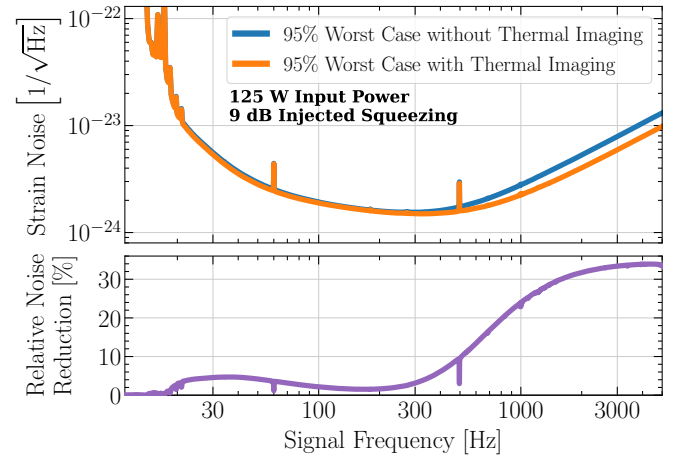


FIG. 4. Comparison of the worst-case strain sensitivities of a LIGO A+ detector, at 95% confidence, with and without thermal-imaging-based inference. These two cases correspond to the two cases denoted by the dashed vertical lines in Fig. 3.

We find that the higher-precision inference enabled by the thermal imaging results in a dramatic narrowing of the range of possible outcomes, significantly improving the *worst* possible sensitivity outcome at 95% confidence.

This large difference in worst-case scenarios translates directly into a statistical improvement in the expected strain sensitivity of the detector, which is shown in Fig. 4 for the worst observed outcomes in 95% of trials. That is, with 95% confidence, the detector will achieve *at least* the strain sensitivity indicated by these curves. Each case assumes the nominal A+ input power of 125 W and an effective injected level of 9 dB of frequency-dependent squeezing, as well as the nominal A+ thermal and technical noise contributions which are combined with the quantum noise curves calculated using FINESSE. We find

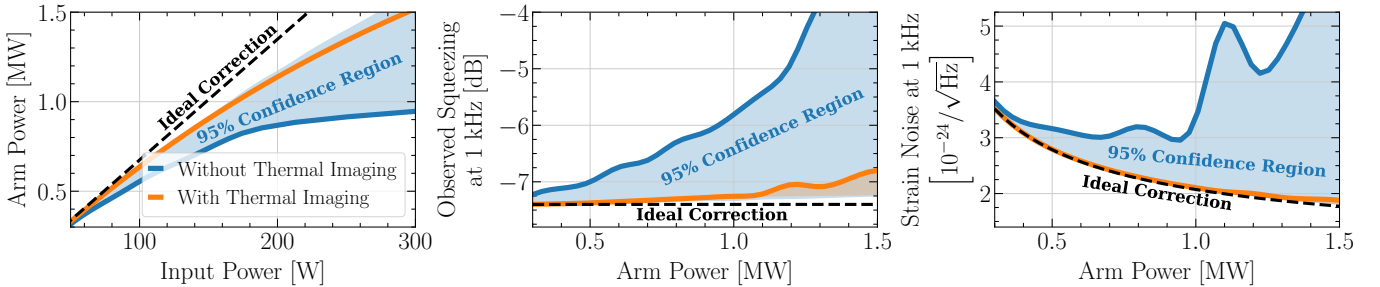


FIG. 5. Projected performance of a LIGO A+ detector as the arm power is increased beyond the nominal target of 750 kW, toward the megawatt scale required for next-generation detectors. The shaded regions indicate the range of possible outcomes, at 95% confidence, for the cases with and without thermal imaging. The dashed lines represent perfect wavefront correction.

that thermal imaging of the test masses can enable up to a 34% greater reduction of the noise floor in LIGO A+, with maximum impact at the highest frequencies, corresponding to an increase of 11 Mpc in the sky-averaged detection range for binary neutron star mergers.

Finally, Fig. 5 shows the detector’s projected performance as the laser power is raised *beyond* the nominal A+ arm power target of 750 kW, towards the higher power levels required for LIGO A# and Cosmic Explorer. Each panel contains two shaded regions representing the range of outcomes spanned by the best 95% of trials in each of the two cases, with (orange) and without (blue) thermal imaging of the test masses. The left panel compares the possible ranges of input power required to achieve a given arm power, at 95% confidence. The middle and right panels compare the ranges of possible squeezing and strain sensitivity outcomes, for a given arm power level, at 95% confidence. Without the new inferential capabilities provided by thermal imaging, the probability of significant squeezing and power degradations grows rapidly above 750 kW, which is exacerbated by higher-order spatial modes becoming co-resonant in the recycling cavities with the changing thermal state of the ITMs. With the new sensing capabilities, the quantum noise performance is limited only by the intrinsic capability of the wavefront actuators to match the spatial profiles of the distortions.

V. DISCUSSION

Our analysis shows that real-time precision inference of the thermal state of the optics is vital to achieving greater quantum-limited sensitivity in gravitational-wave detectors. We have demonstrated that front-surface thermal imaging offers a practical solution. The requirements for full-aperture wavefront correction are most stringent for the ITMs, due to wavefront distortions shifting the higher-order mode resonances of the signal recycling cavity [20], and the sensing requirements identified in this letter can satisfy them. Our assumption of a thermal steady-state FEA model is a realistic assumption for future detectors. The LIGO A+ upgrades include an offline 10.6- μm laser heating system for each ITM, known as the Central HEater for Transient Attenuation (CHETA) [32], designed to maintain the thermal steady state of the optic when the main laser beam is not present due to lock loss. We anticipate that such an offline heating system will be extended to all four test masses by LIGO A# and will be incorporated into the baseline Cosmic Explorer design. The impact of this work will thus extend far beyond A+, as it also delivers a key enabling sensing capability for next-generation gravitational-wave observatories.

ACKNOWLEDGMENTS

The authors thank Georgia Mansell and the Cosmic Explorer mode sensing and control (MSC) design team for helpful comments during the preparation of this manuscript. This material is based upon work supported by the National Science Foundation (NSF) under Award Nos. PHY-2309006 and PHY-2409496. This paper carries LIGO Document Number LIGO-P2500333.

[1] B. P. Abbott *et al.* (LIGO Scientific Collaboration and Virgo Collaboration), Observation of gravitational waves from a binary black hole merger, *Phys. Rev. Lett.* **116**, 061102 (2016).

[2] B. P. Abbott *et al.* (LIGO Scientific Collaboration and Virgo Collaboration), GWTC-1: A Gravitational-Wave Transient Catalog of Compact Binary Mergers Observed by LIGO and Virgo during the First and Second Observ-

- ing Runs, *Phys. Rev. X* **9**, 031040 (2019).
- [3] R. Abbott *et al.* (LIGO Scientific Collaboration and Virgo Collaboration), GWTC-2: Compact Binary Coalescences Observed by LIGO and Virgo during the First Half of the Third Observing Run, *Phys. Rev. X* **11**, 021053 (2021).
- [4] R. Abbott *et al.* (The LIGO Scientific Collaboration and the Virgo Collaboration), GWTC-2.1: Deep extended catalog of compact binary coalescences observed by LIGO and Virgo during the first half of the third observing run, *Phys. Rev. D* **109**, 022001 (2024).
- [5] R. Abbott *et al.* (LIGO Scientific Collaboration, Virgo Collaboration, and KAGRA Collaboration), GWTC-3: Compact Binary Coalescences Observed by LIGO and Virgo during the Second Part of the Third Observing Run, *Phys. Rev. X* **13**, 041039 (2023).
- [6] H. Y. Chen, M. Fishbach, and D. E. Holz, A two per cent Hubble constant measurement from standard sirens within five years, *Nature* **562**, 545 (2018).
- [7] W. M. Farr, M. Fishbach, J. Ye, and D. E. Holz, A Future Percent-level Measurement of the Hubble Expansion at Redshift 0.8 with Advanced LIGO, *ApJL* **883**, L42 (2019).
- [8] K. Skenderis and M. Taylor, The fuzzball proposal for black holes, *Phys. Rep.* **467**, 117 (2008).
- [9] V. Cardoso and P. Pani, Tests for the existence of black holes through gravitational wave echoes, *Nat. Astron.* **1**, 586 (2017).
- [10] R. Brustein and A. J. M. Medved, Quantum hair of black holes out of equilibrium, *Phys. Rev. D* **97**, 044035 (2018).
- [11] D. Tsang, J. S. Read, T. Hinderer, A. L. Piro, and R. Bondarescu, Resonant Shattering of Neutron Star Crusts, *Phys. Rev. Lett.* **108**, 011102 (2012).
- [12] L. Barsotti, L. McCuller, M. Evans, and P. Fritschel, *The A+ design curve*, LIGO Technical Report LIGO-T1800042 (2018).
- [13] P. Fritschel, K. Kuns, J. Driggers, A. Effler, B. Lantz, D. Ottaway, S. Ballmer, K. Dooley, R. X. Adhikari, M. Evans, B. Farr, G. Gonzalez, P. Schmidt, and S. Raja, *Report of the LSC Post-O5 Study Group*, LIGO Technical Report LIGO-T2200287 (2022).
- [14] LIGO Scientific Collaboration, *The LSC Instrument Science White Paper (2025 edition)*, LIGO Technical Report LIGO-T2400407 (2024).
- [15] L. McCuller, S. E. Dwyer, A. C. Green, H. Yu, K. Kuns, L. Barsotti, C. D. Blair, D. D. Brown, A. Effler, M. Evans, A. Fernandez-Galiana, P. Fritschel, V. V. Frolov, N. Kijbunchoo, G. L. Mansell, F. Maticichard, N. Mavalvala, D. E. McClelland, T. McRae, A. Mullavey, D. Sigg, B. J. J. Slagmolen, M. Tse, T. Vo, R. L. Ward, C. Whittle, R. Abbott, C. Adams, R. X. Adhikari, A. Ananyeva, S. Appert, K. Arai, J. S. Areeda, Y. Asali, S. M. Aston, C. Austin, A. M. Baer, M. Ball, S. W. Ballmer, S. Banagiri, D. Barker, J. Bartlett, B. K. Berger, J. Betzwieser, D. Bhattacharjee, G. Billingsley, S. Biscans, R. M. Blair, N. Bode, P. Booker, R. Bork, A. Bramley, A. F. Brooks, A. Buikema, C. Cahillane, K. C. Cannon, X. Chen, A. A. Ciobanu, F. Clara, C. M. Compton, S. J. Cooper, K. R. Corley, S. T. Countryman, P. B. Covas, D. C. Coyne, L. E. H. Datrier, D. Davis, C. Di Fronzo, K. L. Dooley, J. C. Driggers, T. Etzel, T. M. Evans, J. Feicht, P. Fulda, M. Fyffe, J. A. Giaime, K. D. Giardina, P. Godwin, E. Goetz, S. Gras, C. Gray, R. Gray, E. K. Gustafson, R. Gustafson, J. Hanks, J. Hanson, T. Hardwick, R. K. Hasskew, M. C. Heintze, A. F. Helmling-Cornell, N. A. Holland, J. D. Jones, S. Kandhasamy, S. Karki, M. Kasprzack, K. Kawabe, P. J. King, J. S. Kissel, R. Kumar, M. Landry, B. B. Lane, B. Lantz, M. Laxen, Y. K. Lecoeuche, J. Leviton, J. Liu, M. Lormand, A. P. Lundgren, R. Macas, M. MacInnis, D. M. Macleod, S. Márka, Z. Márka, D. V. Martynov, K. Mason, T. J. Massinger, R. McCarthy, S. McCormick, J. McIver, G. Mendell, K. Merfeld, E. L. Merilh, F. Meylahn, T. Mistry, R. Mittleman, G. Moreno, C. M. MowLowry, S. Mozzon, T. J. N. Nelson, P. Nguyen, L. K. Nuttall, J. Oberling, R. J. Oram, C. Osthelder, D. J. Ottaway, H. Overmier, J. R. Palamos, W. Parker, E. Payne, A. Pele, R. Penhorwood, C. J. Perez, M. Pirello, H. Radkins, K. E. Ramirez, J. W. Richardson, K. Riles, N. A. Robertson, J. G. Rollins, C. L. Romel, J. H. Romie, M. P. Ross, K. Ryan, T. Sadecki, E. J. Sanchez, L. E. Sanchez, T. R. Saravanan, R. L. Savage, D. Schaetzl, R. Schnabel, R. M. S. Schofield, E. Schwartz, D. Sellers, T. Shaffer, J. R. Smith, S. Soni, B. Sorazu, A. P. Spencer, K. A. Strain, L. Sun, M. J. Szczepańczyk, M. Thomas, P. Thomas, K. A. Thorne, K. Toland, C. I. Torrie, G. Traylor, A. L. Urban, G. Vajente, G. Valdes, D. C. Vander-Hyde, P. J. Veitch, K. Venkateswara, G. Vengopal, A. D. Viets, C. Vorvick, M. Wade, J. Warner, B. Weaver, R. Weiss, B. Willke, C. C. Wipf, L. Xiao, H. Yamamoto, H. Yu, L. Zhang, M. E. Zucker, and J. Zweizig, LIGO’s quantum response to squeezed states, *Phys. Rev. D* **104**, 062006 (2021).
- [16] D. Ganapathy, W. Jia, M. Nakano, V. Xu, N. Aritomi, T. Cullen, N. Kijbunchoo, S. E. Dwyer, A. Mullavey, L. McCuller, R. Abbott, I. Abouelfettouh, R. X. Adhikari, A. Ananyeva, S. Appert, K. Arai, S. M. Aston, M. Ball, S. W. Ballmer, D. Barker, L. Barsotti, B. K. Berger, J. Betzwieser, D. Bhattacharjee, G. Billingsley, S. Biscans, N. Bode, E. Bonilla, V. Bossilkov, A. Branch, A. F. Brooks, D. D. Brown, J. Bryant, C. Cahillane, H. Cao, E. Capote, F. Clara, J. Collins, C. M. Compton, R. Cottingham, D. C. Coyne, R. Crouch, J. Csizmazia, L. P. Dartez, N. Demos, E. Dohmen, J. C. Driggers, A. Effler, A. Ejlli, T. Etzel, M. Evans, J. Feicht, R. Frey, W. Frischhertz, P. Fritschel, V. V. Frolov, P. Fulda, M. Fyffe, B. Gateley, J. A. Giaime, K. D. Giardina, J. Glanzer, E. Goetz, R. Goetz, A. W. Goodwin-Jones, S. Gras, C. Gray, D. Griffith, H. Grote, T. Guidry, E. D. Hall, J. Hanks, J. Hanson, M. C. Heintze, A. F. Helmling-Cornell, N. A. Holland, D. Hoyland, H. Y. Huang, Y. Inoue, A. L. James, A. Jennings, S. Karat, S. Karki, M. Kasprzack, K. Kawabe, P. J. King, J. S. Kissel, K. Komori, A. Kontos, R. Kumar, K. Kuns, M. Landry, B. Lantz, M. Laxen, K. Lee, M. Lesovsky, F. Llamas, M. Lormand, H. A. Loughlin, R. Macas, M. MacInnis, C. N. Makarem, B. Mannix, G. L. Mansell, R. M. Martin, K. Mason, F. Maticichard, N. Mavalvala, N. Maxwell, G. McCarrol, R. McCarthy, D. E. McClelland, S. McCormick, T. McRae, F. Mera, E. L. Merilh, F. Meylahn, R. Mittleman, D. Moraru, G. Moreno, T. J. N. Nelson, A. Neunzert, J. Notte, J. Oberling, T. O’Hanlon, C. Osthelder, D. J. Ottaway, H. Overmier, W. Parker, A. Pele, H. Pham, M. Pirello, V. Quetschke, K. E. Ramirez, J. Reyes, J. W. Richardson, M. Robinson, J. G. Rollins, C. L. Romel, J. H. Romie, M. P. Ross, K. Ryan, T. Sadecki, A. Sanchez, E. J. Sanchez, L. E. Sanchez, R. L. Savage, D. Schaetzl, M. G. Schiworski,

- R. Schnabel, R. M. S. Schofield, E. Schwartz, D. Sellers, T. Shaffer, R. W. Short, D. Sigg, B. J. J. Slagmolen, C. Soike, S. Soni, V. Srivastava, L. Sun, D. B. Tanner, M. Thomas, P. Thomas, K. A. Thorne, C. I. Torrie, G. Traylor, A. S. Ubhi, G. Vajente, J. Vanosky, A. Vecchio, P. J. Veitch, A. M. Vibhute, E. R. G. von Reis, J. Warner, B. Weaver, R. Weiss, C. Whittle, B. Willke, C. C. Wipf, H. Yamamoto, L. Zhang, and M. E. Zucker (LIGO O4 Detector Collaboration), Broadband quantum enhancement of the LIGO detectors with frequency-dependent squeezing, *Phys. Rev. X* **13**, 041021 (2023).
- [17] M. Evans, R. X. Adhikari, C. Afle, S. W. Ballmer, S. Biscoveanu, S. Borhanian, D. A. Brown, Y. Chen, R. Eisenstein, A. Gruson, A. Gupta, E. D. Hall, R. Huxford, B. Kamai, R. Kashyap, J. S. Kissel, K. Kuns, P. Landry, A. Lenon, G. Lovelace, L. McCuller, K. Ng, A. H. Nitz, J. Read, B. S. Sathyaprakash, D. H. Shoemaker, B. Slagmolen, J. R. Smith, V. Srivastava, L. Sun, S. Vitale, and R. Weiss, *A Horizon Study for Cosmic Explorer: Science, Observatories, and Community*, arXiv e-Print 2109.09882 (2021) [arXiv:2109.09882 \[astro-ph.IM\]](https://arxiv.org/abs/2109.09882).
- [18] C. M. Caves, K. S. Thorne, R. W. P. Drever, V. D. Sandberg, and M. Zimmermann, On the measurement of a weak classical force coupled to a quantum-mechanical oscillator. I. Issues of principle, *Rev. Mod. Phys.* **52**, 341 (1980).
- [19] C. M. Caves, Quantum-mechanical noise in an interferometer, *Phys. Rev. D* **23**, 1693 (1981).
- [20] H. T. Cao, A. Brooks, K. Kuns, D. Brown, H. Yamamoto, and J. W. Richardson, *Post-O5 Thermal Modeling: A# TCS Requirements*, LIGO Technical Report LIGO-G2300624 (2023).
- [21] L. Tao, M. Bhattacharya, P. Carney, L. M. Gutierrez, L. Johnson, S. Levin, C. Liang, X. Ma, M. Padilla, T. Rosauer, A. Wilkin, and J. W. Richardson, Expanding the quantum-limited gravitational-wave detection horizon, *Phys. Rev. Lett.* **134**, 051401 (2025).
- [22] A. F. Brooks, B. Abbott, M. A. Arain, G. Ciani, A. Cole, G. Grabeel, E. Gustafson, C. Guido, M. Heintze, A. Hepstonstall, M. Jacobson, W. Kim, E. King, A. Lynch, S. O'Connor, D. Ottaway, K. Mailand, G. Mueller, J. Munch, V. Sannibale, Z. Shao, M. Smith, P. Veitch, T. Vo, C. Vorvick, and P. Willems, Overview of Advanced LIGO adaptive optics, *Appl. Opt.* **55**, 8256 (2016).
- [23] L. van der Schaaf, K. Agatsuma, M. van Beuzekom, M. Gebyehu, and J. van den Brand, Advanced Virgo phase cameras, *Journal of Physics: Conference Series* **718**, 072008 (2016).
- [24] A. F. Brooks, B. Abbott, M. A. Arain, G. Ciani, A. Cole, G. Grabeel, E. Gustafson, C. Guido, M. Heintze, A. Hepstonstall, M. Jacobson, W. Kim, E. King, A. Lynch, S. O'Connor, D. Ottaway, K. Mailand, G. Mueller, J. Munch, V. Sannibale, Z. Shao, M. Smith, P. Veitch, T. Vo, C. Vorvick, and P. Willems, Overview of Advanced LIGO adaptive optics, *Appl. Opt.* **55**, 8256 (2016).
- [25] T. Rosauer, H. T. Cao, M. Bhattacharya, P. Carney, L. Johnson, S. Levin, C. Liang, X. Ma, L. Martin Gutierrez, M. Padilla, L. Tao, A. Wilkin, A. Brooks, and J. W. Richardson, Demonstration of Next-Generation Wavefront Actuator for Gravitational-Wave Detection, *Optica* (2025), under review.
- [26] S. Melo, *Point absorber investigation*, Virgo Logbook aLOG-66886 (2025).
- [27] K. Izumi and D. Sigg, Advanced LIGO: length sensing and control in a dual recycled interferometric gravitational wave antenna, *Class. Quantum Grav.* **34**, 015001 (2017).
- [28] D. D. Brown, P. Jones, S. Rowlinson, S. Leavey, A. C. Green, D. Töyrä, and A. Freise, PYKAT: Python package for modelling precision optical interferometers, *SoftwareX* **12**, 100613 (2020).
- [29] J. Betzwieser and A. Effler, *ETMY camera calibration*, aLIGO LLO Logbook aLOG-54518 (2020).
- [30] E. Capote, W. Jia, N. Aritomi, M. Nakano, V. Xu, R. Abbott, I. Abouelfettouh, R. X. Adhikari, A. Ananyeva, S. Appert, S. K. Apple, K. Arai, S. M. Aston, M. Ball, S. W. Ballmer, D. Barker, L. Barsotti, B. K. Berger, J. Betzwieser, D. Bhattacharjee, G. Billingsley, S. Biscans, C. D. Blair, N. Bode, E. Bonilla, V. Bossilkov, A. Branch, A. F. Brooks, D. D. Brown, J. Bryant, C. Cahillane, H. Cao, F. Clara, J. Collins, C. M. Compton, R. Cottingham, D. C. Coyne, R. Crouch, J. Csizmazia, A. Cumming, L. P. Dartez, D. Davis, N. Demos, E. Dohmen, J. C. Driggers, S. E. Dwyer, A. Effler, A. Ejlli, T. Etzel, M. Evans, J. Feicht, R. Frey, W. Frischhertz, P. Fritschel, V. V. Frolov, M. Fuentes-Garcia, P. Fulda, M. Fyffe, D. Ganapathy, B. Gateley, T. Gayer, J. A. Giaime, K. D. Giardina, J. Glanzer, E. Goetz, R. Goetz, A. W. Goodwin-Jones, S. Gras, C. Gray, D. Griffith, H. Grote, T. Guidry, J. Gurs, E. D. Hall, J. Hanks, J. Hanson, M. C. Heintze, A. F. Helmling-Cornell, N. A. Holland, D. Hoyland, H. Y. Huang, Y. Inoue, A. L. James, A. Jamies, A. Jennings, D. H. Jones, H. B. Kabagoz, S. Karat, S. Karki, M. Kasprzack, K. Kawabe, N. Kijbunchoo, P. J. King, J. S. Kissel, K. Komori, A. Kontos, R. Kumar, K. Kuns, M. Landry, B. Lantz, M. Laxen, K. Lee, M. Lesovsky, F. L. Villarreal, M. Lormand, H. A. Loughlin, R. Macas, M. MacInnis, C. N. Makarem, B. Mannix, G. L. Mansell, R. M. Martin, K. Mason, F. Matichard, N. Mavalvala, N. Maxwell, G. McCarrol, R. McCarthy, D. E. McClelland, S. McCormick, T. McRae, F. Mera, E. L. Merill, F. Meylahn, R. Mittleman, D. Moraru, G. Moreno, A. Mullavey, T. J. N. Nelson, A. Neunzert, J. Notte, J. Oberling, T. O'Hanlon, C. Ostheder, D. J. Ottaway, H. Overmier, W. Parker, O. Patane, A. Pele, H. Pham, M. Pirello, J. Pullin, V. Quetschke, K. E. Ramirez, K. Ransom, J. Reyes, J. W. Richardson, M. Robinson, J. G. Rollins, C. L. Romel, J. H. Romie, M. P. Ross, K. Ryan, T. Sadecki, A. Sanchez, E. J. Sanchez, L. E. Sanchez, R. L. Savage, D. Schaetzl, M. G. Schiowroski, R. Schnabel, R. M. S. Schofield, E. Schwartz, D. Sellers, T. Shaffer, R. W. Short, D. Sigg, B. J. J. Slagmolen, C. Soike, S. Soni, V. Srivastava, L. Sun, D. B. Tanner, M. Thomas, P. Thomas, K. A. Thorne, M. R. Todd, C. I. Torrie, G. Traylor, A. S. Ubhi, G. Vajente, J. Vanosky, A. Vecchio, P. J. Veitch, A. M. Vibhute, E. R. G. von Reis, J. Warner, B. Weaver, R. Weiss, C. Whittle, B. Willke, C. C. Wipf, J. L. Wright, H. Yamamoto, L. Zhang, and M. E. Zucker, Advanced LIGO detector performance in the fourth observing run, *Phys. Rev. D* **111**, 062002 (2025).
- [31] G. Billingsley, *aLIGO COC Testing and Commissioning Documentation*, LIGO Technical Report LIGO-E1000763 (2023).
- [32] V. Jaberian Hamedan, C. Zhao, L. Ju, C. Blair, and D. G. Blair, Suppression of thermal transients in ad-

vanced LIGO interferometers using CO₂ laser preheat-
ing, [Classical and Quantum Gravity 35, 115006 \(2018\)](#).